Mechanics of Micropattern-Guided Formation of Elastic Surface Instabilities on the Polydimethylsiloxane Bilayer

Zhuofan Qin[1,2⊥], Wentao Xu[1,2*⊥], Ding Wang[2], Yunhong Jiang[2], Linhua Zhu[3], Xue Chen[2], Yifan Li[2], Xuehua Zhang[4], Chunjiang Jia[5] and Ben Bin Xu[1,2*]

[1]School of Mechatronics and Mould Engineering, Taizhou Vocational College of Science and Technology, Zhejiang 318020, China

[2]Mechanical and Construction Engineering, Faculty of Engineering and Environment, Northumbria University, Newcastle upon Tyne, NE1 8ST, UK

[3]College of Chemistry and Chemical Engineering, Hainan Normal University, Key Laboratory of Water Pollution Treatment and Resource Reuse of Hainan Province, Haikou 571158, P.R. China

[4]Department of Chemical and Materials Engineering, University of Alberta, 9211 116 Street NW, Edmonton, Alberta, T6G 1H9, Canada

[5] Offshore House, Albert Street, Blyth, NE24 1LZ, UK

*Email: ycqxwt@gmail.com; ben.xu@northumbria.ac.uk

⊥These authors contributed equally to this work.

Abstract:

The surface buckling on elastic bilayer towards a higher tuneable morphological transition has attracted considerable interests. While there are many studies on the 2-dimensional analysis of surface topological changes under uniaxial plain strain, the mechanism of bifurcation remains to be understood. In this work, we investigate the surface wrinkling and the post-wrinkling bifurcation on the thin film bilayer with a micropattern configuration at a 3-dimensional level. The pattern present on the surface of hyper-elastic polydimethylsiloxane (PDMS) bilayer on micron scale, providing a local confinement to regulate the planar strain energy distribution. Therefore, a dedicated transition from wrinkle to post-wrinkling morphologies can be programmed. Finite element analysis further reveals that such pattern guided post-wrinkling bifurcation (i.e., main crease near the pattern edge) is caused by the stress concentration at the edge of micropattern. The simulation results uncover several subcritical features for the generation of creases: upon releasing (i.e., decreasing the overall compressive strain), they do not recover to the doubling of wrinkles at the strain level when they initiate, and a significant hysteresis is resulted. This finding will open a new window on designing and developing future smart surfaces, sensors and actuators.

1. Introduction

Structural surfaces with dedicated functions are useful in various engineering fields [1-4]. The surface that can respond to external stimuli is of particular interest, as it can be readily designed and controlled [5, 6]. One type of structural surface is the patterned surface on bilayer/multilayer system with reversible elastic instabilities [7-11]. Notable progresses in understanding the underlying mechanics of elastic instabilities [12-14] have enabled applications in actuators [15], optical shutters [16], self-accommodated structure [17], sensors [18-20], etc. An important aspect for practical implementation of active soft matter in developing actuators and soft robots, is to harness the responsive properties in a controllable manner. Understanding the mechanics of deformation and the transformative behavior associated with different actuation methods (compression in this paper), is of great significance in this context [21-27]. The phenomena of elastic instability have already been observed and extensively investigated in numerous prior studies with different elastic materials [28-30]. However, the primary focus of this paper pertains solely to PDMS, a material exhibiting rubber-like properties [31-36]. However, considerable knowledge gap remains to be bridged regarding to the controllable formation and the configurability of desired morphologies.

Upon compressing the elastomer bilayer in conjunction with a stiff skin layer, the formation of surface wrinkles mitigates the in-plane compression of skin layer by leveraging the favourable bending mechanism. Subject to the further compression, the surface wrinkles undergo a series of bifurcation, which may or may not appear in sequence of period-doubling [37], quadrupling [38], and the ultimate emergence of deep folds and/or creases [39-42]. The mechanism that governs these wrinkling and post-wrinkling phenomena has been associated with the intrinsic material properties, such as modulus disparities [43] and Poisson's ratio [44], as well as structural variables, e.g., thickness [45] and the pre-strain condition [46]. However, previous studies of compressive instabilities mostly focused on either non-patterned surface

systems or those ones where the mechanism can be modelled as a two-dimensional bilayer system [47]. Whitesides et al reported a fundamental phenomenon of patterns on the surface of a bilayer structure in an experimental setting [12, 48]. One flat bilayer system, recent research considered adhesion energy of two layers based on thermodynamics and the 3 dimensional (3D) phase diagram which contained not only the previously stated typical morphologies but also the delaminated buckles was summarized by parameters such as: mismatch strain, modulus ratio and normalized adhesion energy between two layers [49, 50]. In further researches, the phase diagram of particular bifurcations was investigated by dimensionless parameters on both flat and curved bilayer system [51]. But the mechanics of bifurcation of elastic instability on patterned surface remains yet to be explored.

The functional materials can essentially offer a variety of possibilities on the designability and configures of devices [52-55]. A controllable formation of elastic instabilities is crucial for various applications in the biomedical applications [56], wearable devices [57], microfluidics [17], and sensors [18-20]. Our group developed an experimental strategy [58] to create 2D harmonic surface wrinkle patterns and control transition thresholds on the surface of an elastic bilayer of polydimethylsiloxane(PDMS). The space lattice perforations lead to the emergence of harmonious wrinkle networks as a result of confinement. However, the dynamics of initiating planar wrinkle patterns and localized wrinkle-crease transitions at 3D level has not been fully understood.

In this study, we investigate the mechanics of surface instabilities and the dynamic evolution between each state, i.e., the wrinkles, period-doubling and creases, on an elastic surface using a 3D finite element method (FEM). Our investigation focuses on the system distinct from conventional bilayer structures. The system consists of a stiff skin and a compliant substrate, with space lattice micropatterns introduced on the surface of stiff film. The distribution and evolution of system morphology are closely monitored and discussed both

theoretically and experimentally. The discussion on hysteresis during the loading/unloading process unveils insights between the visco-elastic nature of materials and the configured instability morphologies. The results are expected to guide the design and develop the future flexible/wearable electronics as well as the Human Machine Interface.

2. Methodology

PDMS, a conventional hyper-elastic elastomer [48, 59-61], was used for constructing bilayer system in the experiments. With the plasma treatment, a stiff skin layer was formed on the top of PDMS layer. By affixing the bilayer structure onto a pre-stretched thick elastomer foundation layer, equivalent compression can be achieved by gradually releasing the base, as illustrated in Figure 1a and Movie S1.

The theoretical study was mostly carried by Abaqus, with implementing the finite element method (FEM). The sandwich panel structure was constructed to host the elastic instability [62-64]. Subject to continuous uniaxial compression, the wrinkling and buckling appeared on bilayer following a sequential order, which was determined by the material properties, dimensions of the system predicted by Koiter's method and linear perturbation analysis [65, 66]. The model considered fully tied substrate and film with no delamination or shear stress between them. The resulting surface pattern exhibited an almost sinusoidal curve, with characteristics such as wavelength λ and amplitude A that can be used for characterization and analysis for a small range of deformation. The critical strain ε_c, plain elastic modulus $\bar{E}_s$ of the substrate and $\bar{E}_f$ top thin film, the thickness h of top thin film, are identified in Figure S1. The equations (Eq 1-4) describe the material parameters and their effects on the wrinkling behaviour. For the post-wrinkling phenomenon, two distinct types of bifurcations were recorded: period-doubling and creasing. The merging of waves occurs, resulting in an increase

in the wavelength of each wave, while the amplitudes exhibit separate increasing and decreasing trends [43].

$$\varepsilon_c = \frac{1}{4}\left(\frac{3\bar{E}_s}{\bar{E}_f}\right)^{\frac{2}{3}} \quad (1)$$

$$\lambda = 2\pi h\left(\frac{\bar{E}_f}{3\bar{E}_s}\right)^{\frac{1}{3}} \quad (2)$$

$$A = h\left(\frac{\varepsilon}{\varepsilon_c} - 1\right)^{\frac{1}{2}} \quad (3)$$

$$\bar{E} = E/(1-v^2) \quad (4)$$

For the finite element analysis (FEA), Neo-Hookean model [40, 41, 67] was applied to represent the hyper-elastic material property and simulate the wrinkles and post-wrinkling phenomenon on the bilayer model. Based on PDMS material, the tensile test data was extracted from experiment and imported into an adapted Neo-Hookean model. The stiff oxidized layer was considered as linear elasticity and different Poisson's ratio like glass materials [41, 48]. With the experimental data from tensile tests, the output line fit the corresponding parameters of Neo-Hookean model obtained by constituting the output diagram of corresponding relation between nominal stress and strain (stretching strain is up to 1.65). Poisson's ratio of soft substrate and stiff film was considered to be 0.48 and 0.33, respectively [48]. The adapting result is shown in Figure 1b. The intrinsic hyper-elastic algorithm consists of equation 5-9.

$$U = C_1(\bar{I}_1 - 3) + \frac{1}{D_1}(J^{el} - 1)^2 \quad (5)$$

$$\mu_0 = 2C_1 \quad (6)$$

$$K_0 = \frac{2}{D_1} \quad (7)$$

$$\bar{I}_1 = \bar{\lambda}_1^2 + \bar{\lambda}_2^2 + \bar{\lambda}_3^2 \quad (8)$$

$$\bar{\lambda}_i = J^{-\frac{1}{3}}\lambda_i \quad (9)$$

A corresponding 3D model with the experimental configuration was constructed (Figure 1b and S1). The diameter ϕ, hole distance *D*, thickness of outer hard layer h and bottom soft layer *H* were defined and matched to the value in experimental configuration.

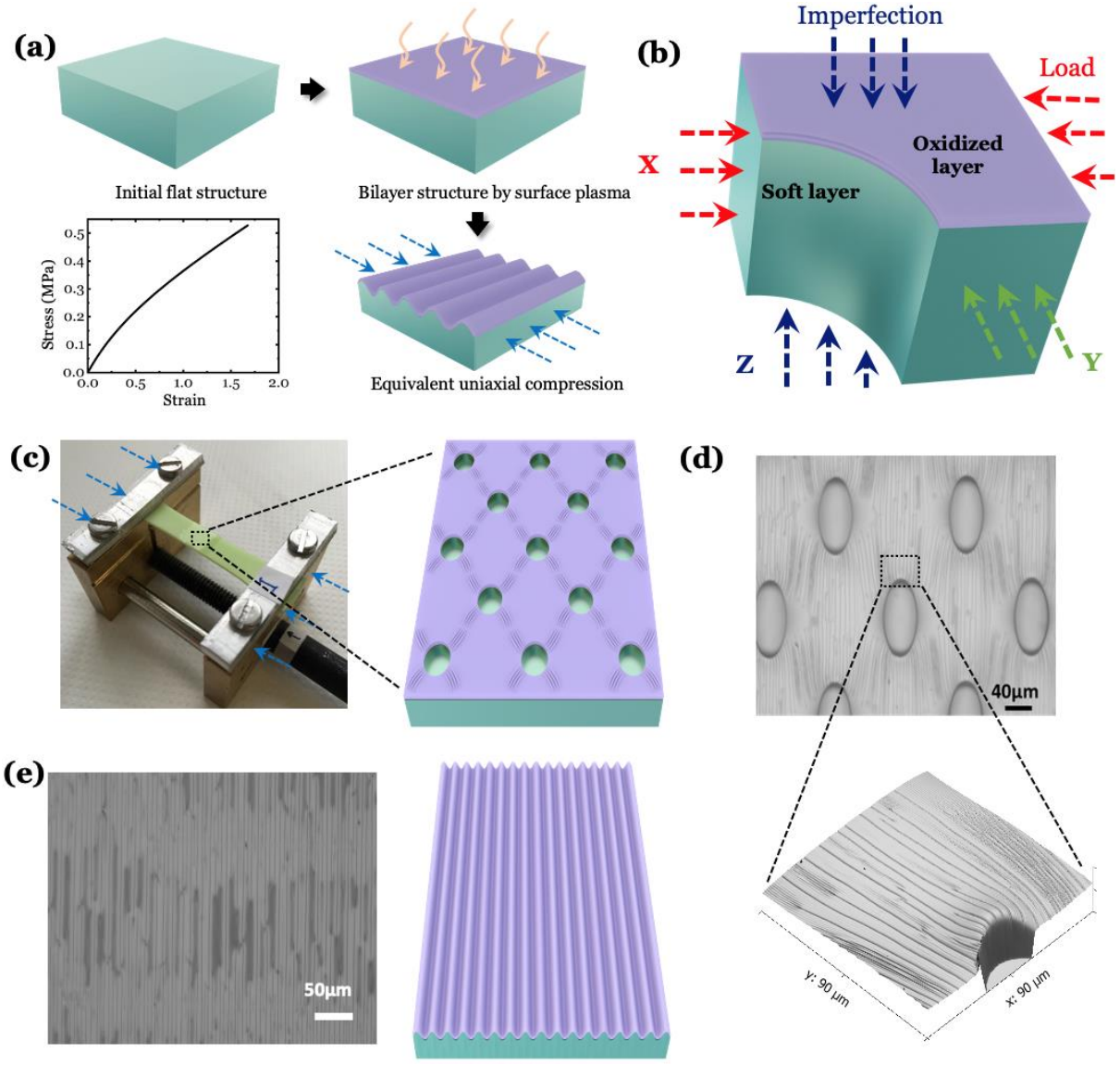

Figure 1 a. Schematic diagram of fabricating the bilayer and Neo-Hookean hyper-elastic plot from the tensile test of PDMS. **b.** Configuration of simulation model. **c.** Experimental setup and illustration of surface morphology. **d.** Initial wrinkles observed by optical microscopy and Atomic Force Microscopy (AFM). **e.** Global wrinkling morphology of conventional non-patterned bilayer.

The plasma oxidation create a skin layer with a small penetration depth of ~100 nm on the PDMS surface, where the PDMS substrate has a thickness of 125 μm [58]. The plasma-treated surface layer was considered as linear elastic [64] with a value of ~ 70 GPa. A typical elastic modulus (1.6 MPa) was assigned for PDMS in this work [43]. The essential parameters used in simulation were detailed in Table 1. By extracting parameters and the stress-strain plot

of the hyper-elastic model, for soft core, the parameters can be acquired as C_1 = 0.1041 MPa, and D_1 = 0.3893 MPa. According to equations 6 and 7, the shear modulus μ_0 = 0.2082 MPa and the bulk modulus = 5.1374 MPa. Based on the isotropic mechanics, equivalent elastic modulus and plain elastic modulus of PDMS can be obtained as 0.6163 MPa and 0.8008 MPa.

Compared with other studies of elastic bilayer system, our work expands the previous 2D configuration into 3D structure with the Neo-Hookean hyperelastic model. Specific definitions of dimension parameters are illustrated in Figure S1. In order to conserve resources, the entire model was perforated with the circular through hole which means the depth of circular hole is same as the thickness of whole model, as only the top region of experimental sample was examined. This differs from the experimental approach, where the entire sample was much thicker and not thoroughly perforated by the circular micropatterns.

Table 1. Values of model parameters.

Model parameter	**Value**
Max applied compressive strain ε_{max}	0.55
Elastic modulus of stiff film E_f	71.36 MPa
Elastic modulus of soft substrate E_s	0.6163 MPa
Poisson's ratio of stiff film	0.33
Poisson's ration of soft substrate	0.48
C_1 in Neo-Hookean model	0.1041 MPa
D_1 in Neo-Hookean model	0.3893 MPa
Thickness of soft substrate h	2.5 μm
Thickness of stiff film H	0.05 μm
Length of quarter model	60 μm
Width of quarter model	60 μm
Pattern/Hole diameter	40 μm

3. Results and discussions

3.1. Construction of 3D model to benchmark the phenomenon

The onset of wrinkling phenomenon takes place once the applied strain reaches the critical threshold, as shown in Figure 1c and 1d. By intentionally incorporating circular patterns onto the PDMS bilayer, a significant disparity in the initial wrinkling morphology under

compression becomes evident (Movie S1 and Figure S2) when compared to the conventional pattern less bilayer configuration shown in Figure 1e. Through planting the micropattern array on the top layer of PDMS bilayer, it will provide a promising direction to enable the future development of microdevices, such as microchannels [68].

To benchmark the wrinkling morphology in 3D model, a quarter model of single circular hole was used to save simulation time and resources, as the morphology is axisymmetric based on the experimental results. For specific boundary conditions, degree of freedom (DOF) in the model is set to X and Y axis shown in Figure 1b. The displacement and rotation along Z axis of bottom substrate are also fixed. The outer hard layer was defined with a self-contact mode which is frictionless. The displacement load is expressed as $u_3 = \xi \cos(\pi X_1/\lambda)$, where u_3 represents the infinitesimal displacement load in the Z direction along the X coordinate position X_1, and the ratio of $\xi/\lambda = 0.005$. Since the 3D simulation has complicated large deformation and self-contact problems which are different from normal 2D simulation, the non-linear dynamic explicit solver (10 step time duration) with mechanical module and C3D8R element was applied for 3D simulation. According to previously reports, the modulus ratio E_f/E_s was set as 100 [58] and the layer thickness ratio of two different materials H/h in the film-substrate model should be more than 50.

3.2. Role of micropatterns in post-wrinkling bifurcation

The primary phenomenon can be experimentally characterized by the sequence of initial wrinkling, period-doubling, and creasing, as depicted in Figure 2a. Subsequent releasing of the bilayer results in a final state not as flat as the initial state, primarily due to the hysteresis, which will be discussed in next section. The generation of sequential instabilities with an increase in the compressive strain is shown in Figures 2b and 2c. The initial wrinkling manifests localization at the top and bottom edges of hole, and progressively evolves into period-doubling and creasing patterns with main big crease near the hole edges (Movie S1 and Figure S2). For

some special micropattern arrays, e.g., square array in Figure 2b, the big crease near the edges can finally evolve to a large folding. Figure 2d shows the surface morphology observed during the release, i.e., decreasing the compressive strain. By comparing the surface morphologies at the same strain in Figures 2c and 2d, it is found that the instability of micro-patterned bilayer surface exhibits significant hysteresis and the structure cannot recover to the initial flat state.

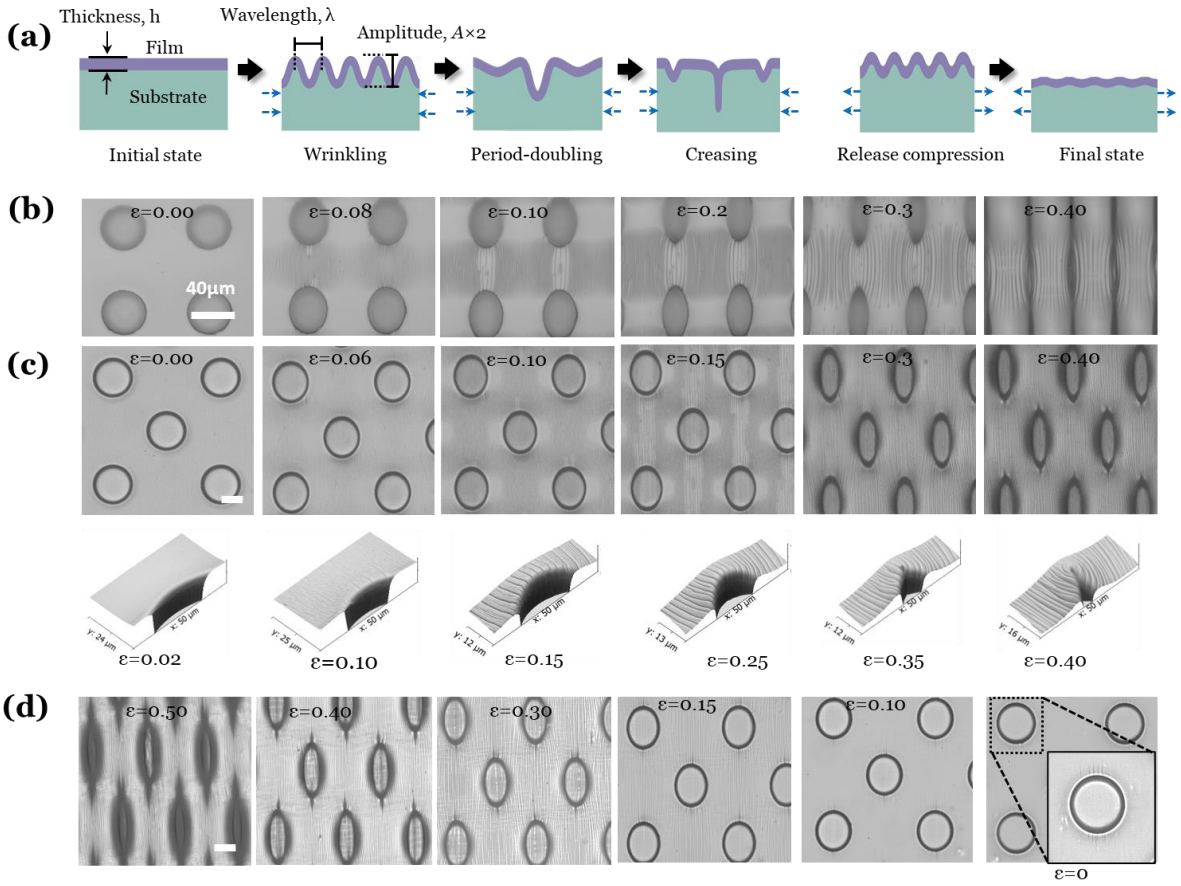

Figure 2 **a.** Illustration of wrinkling, period-doubling, and creasing with gradually increased compression and hysteresis of the instability behaviour in releasing. **b.** Experimental results of the square micro-pattern array under increasing compression. **c.** Experimental results of the diamond micro-pattern array under compressing. **d.** Experimental results of the diamond micro-pattern array under releasing.

For the 3D simulation, the quarter hole model with a compressive strain of up to 0.55 was applied in the step of post-processing, the legend on the left denotes the specific values and distribution of Mises stress for the applied strain ε in Figure 3a, b. The morphology is in

good agreement with the experimental results. When the compressive strain ε is increased to a critical value (e.g., 0.02 in the simulation), uniform wrinkles form at the edge of circular hole first (see Figure 2a), due to that the maximum stress is located at the hole edge shown by the stress distribution in Figure 3a. The critical strain ε_c and the wavelength λ_0 of the initial sinusoidal wrinkle can be estimated by (31-35): $\varepsilon_c = \frac{1}{4}\left(\frac{3\bar{E}_s}{\bar{E}_f}\right)^{\frac{2}{3}}$ and $\lambda_0 = 2\pi h\left(\frac{\bar{E}_f}{3\bar{E}_s}\right)^{\frac{1}{3}}$. Here h is the thickness of stiff film, $\bar{E}_s$ and $\bar{E}_f$ are the plain elastic modulus of substrate and the top film, respectively. By applying the parameter values from Table 1, ε_c and λ_0 can be calculated and compared with the 3D simulation results in Table 2. The values in the table show that 3D simulation results agree well with the numerical theoretical prediction, suggesting that the circular micropatterns do not affect the initial wrinkling, although the wrinkles are not globally distributed on the top surface of the bilayer structure.

Table 2. Parameter comparison of initial wrinkling.

Parameters	**Theoretical value**	**3D Simulation results**
Critical strain ε_c	~0.024	0.02
Initial wavelength λ_0	~1.011μm	~1.01μm

When the compressive strain ε is increased from 0.02 to 0.10, the post-wrinkling bifurcation (namely period-doubling) emerges and grows rapidly (Movie S2). At a strain of 0.04, some wrinkles become deeper, while their neighbours become shallower, resulting in a bifurcation of normalized amplitude (rise and drop at the same stain) of wrinkles, as illustrated in Figure 3c. The amplitude of the deepened wrinkles is denoted as A_1 to denote the crease depth matching the amplitude of previously uniform wrinkles, while the amplitude of the shallowed wrinkles is denoted as A_2. When the compressive strain reaches 0.07, the second bifurcation takes place. Some deepened wrinkles evolve to creases with depth A_1. The amplitude of some other wrinkles decreases due to the mitigation of stain localization, and A_3

is used to denote their amplitude (Figure 3c). It is worth noting that these morphological bifurcations occur significantly earlier than the previous reported data [37], i.e., at lower critical strains (0.04 and 0.07) compared with the reported critical strains (0.15 and 0.22) for the plain bilayer structure in experiment (Figure S3) and critical strains (0.16 and 0.27) in simulation (Figure S4). The micropattern accelerate the onset of post-wrinkling bifurcation during compression, by guiding the strain localization at the pattern edges. When the compressive strain continues to increase from 0.07, no more bifurcation is observed.

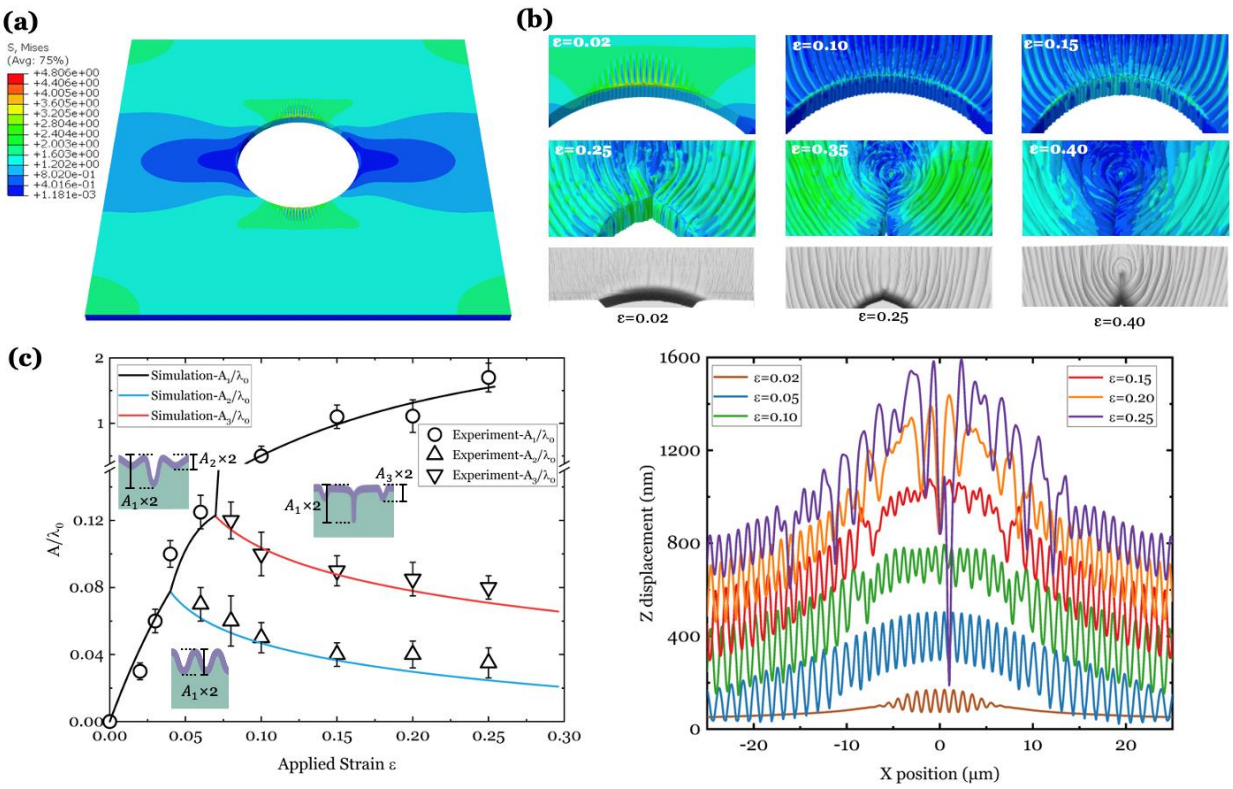

Figure 3 **a.** Simulation result of global morphology at the overall compressive strain ε = 0.02 **b.** Simulation results of local morphology evolution during compression. Experimental results (on third row) are also presented for comparison. **c.** Post-wrinkling bifurcation diagram. Definitions of wrinkle amplitudes and crease depth are shown in the insets. **d.** Deformation profiles of the top surface at different levels of compressive strain.

At a strain of 0.35, the concentration of wrinkles and creases near the pattern/hole edge results in an annular morphology, consistent with the experimental results (see Figure 3b). As the compressive strain progresses to 0.4, the strain localization was developed intensively at

entire annular region. Additional wrinkles located in the vicinity of this region are gradually drawn towards the central closed line. Ultimately, when the strain exceeds 0.5, the hole closes completely. Figure 3d summarizes the deformation profile (i.e., displacement along Z) along X direction from the area near the hole (X = 0) to the edge of whole model. It is seen that deep main crease is formed at the hole edge (e.g., profile at strain of 0.25).

3.3. Hysteresis and reversibility for the micropattern-guided instability

We then investigate the hysteresis of the wrinkling and the associated bifurcations in the experimental results. Figure 4a compares the global surface morphology of bilayer at the same compressive strain (ε = 0.25) during the compression and releasing process. Figure 4b shows the evolution of the local morphology as the strain decreases from 0.25 to 0. An annular distribution of relatively high stress area persists even at low strains during the release process. By analysing the amplitude-to-initial-wavelength ratio A_1/λ_0 in Figure 4c, it is evident that the A_1/λ_0 values during release are significantly higher than those during compression at the same level of strain. The final state characterized by residual wrinkles is different from the initial flat state. The morphology and surface profiles of compression and release process have been compared at different strains (Movie S3 and Figure S4).

Furthermore, we compared three simulation results corresponding to maximum strain of 0.07, 0.25, and 0.55 in the compression-release cycle. At a low maximum strain (e.g., 0.07 in Figure 4c), the crease only initiates and period-doubling exhibits modestly. In this case, the hysteresis during the process of strain release is negligible, in contrast to the significant hysteresis in the case of large maximum strains (e.g., 0.25 and 0.55 in Figure 4c) where deep creases develop near the pattern edges. This indicates that the creases formed in the micro-patterned bilayer structure are subcritical, i.e., exhibiting hysteresis, compared with the simulated hysteresis on flat bilayer (Figure S5 and Movie S4). In Figure 4d the normalized total energy (includes kinetic energy and strain energy) of the whole bilayer system is

compared during compression and release at the same strain levels. In the case of a large maximum strain (e.g., 0.55), the energy difference (energy during compression – that during release) remains positive, indicating that the morphology during release is always at a lower energy state than that during compression. Therefore, the system cannot recover to the initial flat configuration even when the compressive strain is reduced to 0 and large hysteresis is resulted. Conversely, in the case of a small maximum strain (e.g., 0.07 in Figure 4d), the energy difference between compression and release processes is around 0 with little hysteresis.

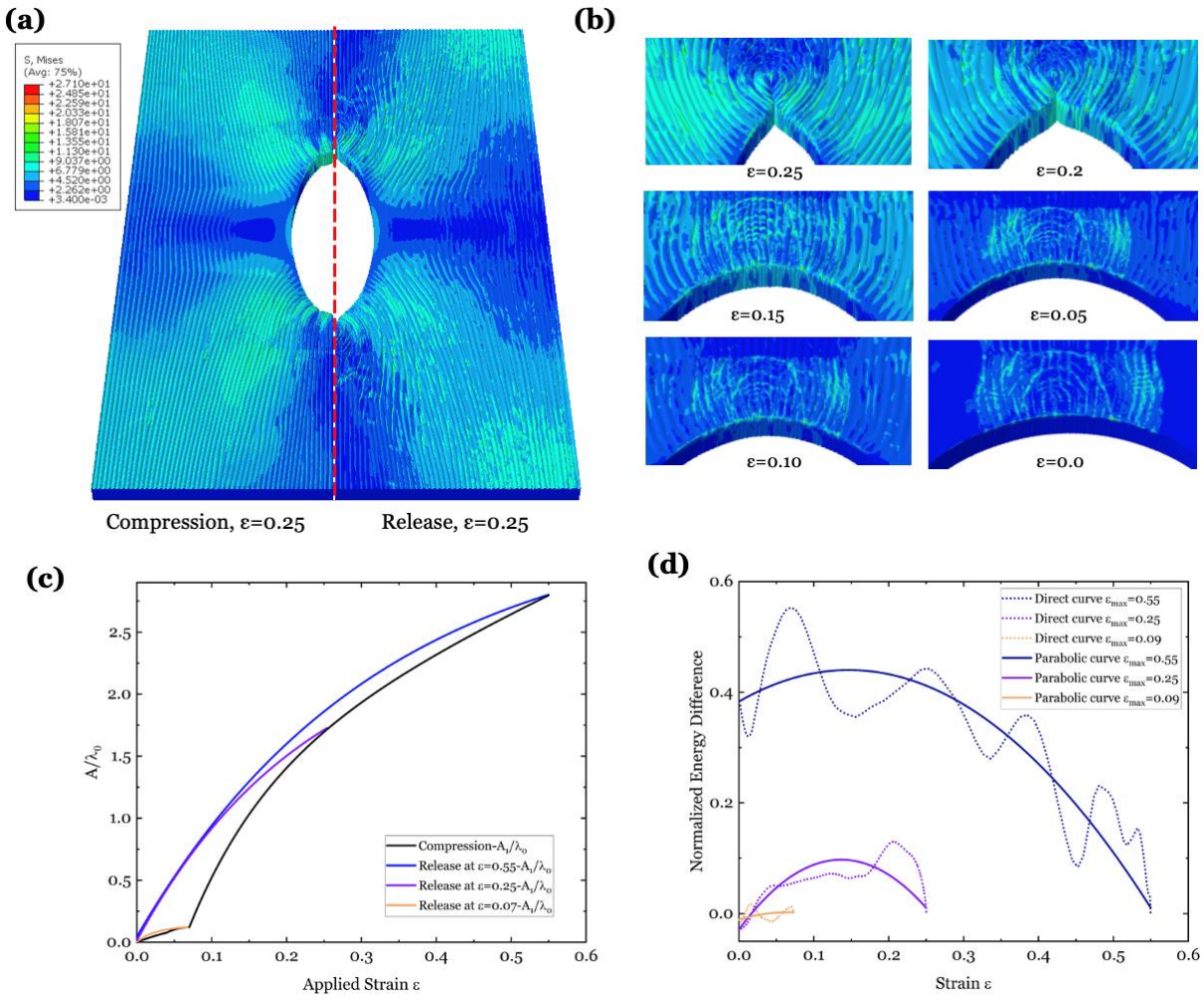

Figure 4 **a.** Comparison of global morphologies during compression and releasing at ε = 0.25. **b.** Evolution of local morphologies during releasing from ε = 0.25 to 0. **c.** Amplitude-to-initial-wavelength ratio (A_1/λ_0) during compression and release **d.** Normalized energy difference of compressing and releasing process by direct curve and parabolic fitting.

4. Conclusions

In summary, we investigate the instability of micro-patterned bilayer structure by both experimental studies and 3D finite element simulations. The post-wrinkling bifurcations (period-doubling and creasing) during compression and the hysteresis during release are observed in the experiments, with a good agreement to the simulation results. The micropattern does not affect the critical strain for the initial onset of wrinkle. However, it accelerates the transitions from the wrinkling to period-doubling (bifurcation) and further to crease, due to stress concentrating at the edge of each pattern hole. Such stress concentrating also leads to the formation of deep crease near the pattern edge. Furthermore, the creases formed in the micro-patterned bilayer system are subcritical and contribute to a significant hysteresis during release. The simulation can predict the behaviour of similar models with different dimensions or materials, thus enabling its universal application in the field of smart micro-surfaces and micro-sensors.

Acknowledgement

Nothing to be acknowledged.

Funding

This work was supported by the Taizhou Science and Technology Plan Projects (Industrial Category) 2022(Grant no. 22gyb23) and Key Research Projects of Taizhou Vocational College of Science and Technology 2022(Grant no. 22NDZD03). Financial supports from the Northumbria University for the RDF studentship are gratefully acknowledged. XHZ acknowledges the support from NSERC-Alberta Innovated Advanced Program. BBX is grateful for the support from the Engineering and Physical Sciences Research Council (EPSRC, UK) grant-EP/N007921.

Author's contribution

Wentao Xu (W.X.), Zhuofan Qin (Z.Q.) and Ding Wang (D.W.) carried the numerical work and data processing, Yunhong Jiang (Y.J.), Linhua Zhu (L.Z.) and Yifan Li (Y.L.) helped in data analysis, Ben Bin Xu designs the work programme with Xue Chen (X.C.), Xuehua Zhang (X.Z.) and Chunjiang Jia (C.J.). All authors contributed in the manuscript drafting.

Conflict of Interest

The authors declare that they have no conflict of interest.

References

1. Yao L, He J (2014) Recent progress in antireflection and self-cleaning technology – from surface engineering to functional surfaces. Progress in Materials Science 61:94-143
2. Malshe A, Rajurkar K, Samant A, Hansen HN, Bapat S, Jiang W (2013) Bio-inspired functional surfaces for advanced applications. CIRP Annals 62:607-628
3. Abdel-Aal HA (2016) Functional surfaces for tribological applications: Inspiration and design. Surface Topography: Metrology and Properties 4:043001
4. Zhang S, Zhou Y, Zhang H, Xiong Z, To S (2019) Advances in ultra-precision machining of micro-structured functional surfaces and their typical applications. International Journal of Machine Tools and Manufacture 142:16-41
5. Petrzhik MI, Levashov EA (2007) Modern methods for investigating functional surfaces of advanced materials by mechanical contact testing. Crystallography Reports 52:966-974
6. Namdari N, Mohammadian B, Jafari P, Mohammadi R, Sojoudi H, Ghasemi H, Rizvi R (2020) Advanced functional surfaces through controlled damage and instabilities. Materials Horizons 7:366-396
7. Yoon J, Ru CQ, Mioduchowski A (2005) Surface instability of a bilayer elastic film due to surface van der waals forces. Journal of Applied Physics 98:113503
8. Mukherjee R, Pangule R, Sharma A, Tomar G (2007) Contact instability of elastic bilayers: Miniaturization of instability patterns. Advanced Functional Materials 17:2356-2364
9. Shi Z, Baumgart T (2014) Dynamics and instabilities of lipid bilayer membrane shapes. Adv Colloid Interface Sci 208:76-88
10. De Domenico M, Nicosia V, Arenas A, Latora V (2015) Structural reducibility of multilayer networks. Nat Commun 6:6864
11. Hammoud Z, Kramer F (2020) Multilayer networks: Aspects, implementations, and application in biomedicine. Big Data Analytics 5:
12. Bowden N, Brittain S, Evans AG, Hutchinson JW, Whitesides GM (1998) Spontaneous formation of ordered structures in thin films of metals supported on an elastomeric polymer. Nature 393:146-149
13. Chen D, Yoon J, Chandra D, Crosby AJ, Hayward RC (2014) Stimuli-responsive buckling mechanics of polymer films. Journal of Polymer Science Part B: Polymer Physics 52:1441-1461
14. Chen D, Cai S, Suo Z, Hayward RC (2012) Surface energy as a barrier to creasing of elastomer films: An elastic analogy to classical nucleation. Phys Rev Lett 109:038001
15. Kim S, Kim W, Kim Y (2020) Design and performance evaluation of thin-film actuators based on flexible ni-co substrates. Micro and Nano Systems Letters 8:
16. Chen S, Liu Z, Du H, Tang C, Ji CY, Quan B, Pan R, Yang L, Li X, Gu C, Zhang X, Yao Y, Li J, Fang NX, Li J (2021) Electromechanically reconfigurable optical nano-kirigami. Nat Commun 12:1299
17. Holmes DP, Tavakol B, Froehlicher G, Stone HA (2013) Control and manipulation of microfluidic flow via elastic deformations. Soft Matter 9:7049-7053
18. Wang C, Wang D, Kozhevnikov V, Dai X, Turnbull G, Chen X, Kong J, Tang BZ, Li Y, Xu BB (2020) A flexible topo-optical sensing technology with ultra-high contrast. Nature Communications 11:1448
19. Muralt P. Piezoelectric and pyroelectric microsystems based on ferroelectric thin films. ISAF '96 Proceedings of the Tenth IEEE International Symposium on Applications of Ferroelectrics. 145-151 (1996)
20. Shi L, Li Z, Chen M, Qin Y, Jiang Y, Wu L (2020) Quantum effect-based flexible and transparent pressure sensors with ultrahigh sensitivity and sensing density. Nat Commun 11:3529
21. Hu F, Wang L, Liu Y, Hessien MM, Azab IHE, Jing S, Elnaggar AY, El-Bahy SM, Huang M, Zhang R (2022) Molecular dynamics simulation and experimental study of 3,5-difluoro-2,4,6-trinitroanisole/2,4,6,8,10,12-hexanitrohexaazaisowurtzitane mixed components. Advanced Composites and Hybrid Materials 5:1307-1318

22. Kost K, Tsaramirsis i, Patel A, Sharma P, Reddy N, R P, hawa h, Tsaramirsis G, Pavlopoulou A, KoÃ§er ZAK, Piromalis D (2021) Bio-virus spread simulation in real 3d space using augmented reality. Engineered Science 16:319-330
23. Huang J, Lu X, Zhang X (2022) Transient computational fluid dynamics simulation of pulse feed in vacuum membrane distillation process. Advanced Composites and Hybrid Materials 5:2515-2526
24. Chen L, Li J, Zhao Y, Li M, Li L, Hou H, Chen L (2021) Numerical simulation and optimization of indirect squeeze casting process. Engineered Science 13:65-70
25. Zhao Z, Liu P, Dang H, Chen Y, Zhang C, Pagani A (2022) Understanding the critical role of boundary conditions in meso-scale finite element simulation of braided composites. Advanced Composites and Hybrid Materials 5:39-49
26. Chen W, Zhao Y, Yang S, Zhang D, Hou H (2021) Three-dimensional phase-field simulations of the influence of diffusion interface width on dendritic growth of fe-0.5 wt.%c alloy. Advanced Composites and Hybrid Materials 4:371-378
27. Liu H, Guo L, Liu M, Chen H, Han W, Bian H, Tian X, Wang C, Guo Z, Sun J (2022) Water management simulation of proton exchange membrane fuel cells with micro-ribs based on volume of fluid model. ES Energy & Environment 15:45-55
28. Meng X, Li Y, AlMasoud N, Wang W, Alomar TS, Li J, Ye X, Algadi H, Seok I, Li H, Xu BB, Lu N, El-Bahy ZM, Guo Z (2023) Compatibilizing and toughening blends of recycled acrylonitrile-butadiene-styrene/recycled high impact polystyrene blends via styrene-butadiene-glycidyl methacrylate terpolymer. Polymer 272:125856
29. Li T, Wei H, Zhang Y, Wan T, Cui D, Zhao S, Zhang T, Ji Y, Algadi H, Guo Z, Chu L, Cheng B (2023) Sodium alginate reinforced polyacrylamide/xanthan gum double network ionic hydrogels for stress sensing and self-powered wearable device applications. Carbohydrate Polymers 309:120678
30. Gao F, Liu Y, Jiao C, El-Bahy SM, Shao Q, El-Bahy ZM, Li H, Wasnik P, Algadi H, Xu BB, Wang N, Yuan Y, Guo Z Fluorine-phosphate copolymerization waterborne acrylic resin coating with enhanced anticorrosive performance. Journal of Polymer Science n/a:
31. Zhang H, Zhang X, Li D, Zhuang J, Liu Y, Liu H, Wu D, Feng J, Sun J (2022) Synergistic enhanced thermal conductivity of polydimethylsiloxane composites via introducing scf and hetero-structured gb@rgo hybrid fillers. Advanced Composites and Hybrid Materials 5:1756-1768
32. Hu M, Gao Y, Jiang Y, Zeng H, Zeng S, Zhu M, Xu G, Sun L (2021) High-performance strain sensors based on bilayer carbon black/pdms hybrids. Advanced Composites and Hybrid Materials 4:514-520
33. Wu H, Sun H, Han F, Xie P, Zhong Y, Quan B, Zhao Y, Liu C, Fan R, Guo Z (2022) Negative permittivity behavior in flexible carbon nanofibers- polydimethylsiloxane films. Engineered Science 17:113-120
34. Jiang N, Hu D, Xu Y, Chen J, Chang X, Zhu Y, Li Y, Guo Z (2021) Ionic liquid enabled flexible transparent polydimethylsiloxane sensors for both strain and temperature sensing. Advanced Composites and Hybrid Materials 4:574-583
35. Liu R, Kim JG, Dhakal P, Li W, Ma J, Hou A, Merkel C, Qiu J, Zoran M, Wang S (2022) Neuromorphic properties of flexible carbon nanotube/polydimethylsiloxane nanocomposites. Advanced Composites and Hybrid Materials 6:14
36. Liu J, Zhang J, Tang J, Pu L, Xue Y, Lu M, Xu L, Guo Z (2020) Polydimethylsiloxane resin nanocomposite coating with alternating multilayer structure for corrosion protection performance. ES Materials & Manufacturing 10:29-38
37. Brau F, Vandeparre H, Sabbah A, Poulard C, Boudaoud A, Damman P (2010) Multiple-length-scale elastic instability mimics parametric resonance of nonlinear oscillators. Nature Physics 7:56-60
38. Auguste A, Jin L, Suo Z, Hayward RC (2017) Post-wrinkle bifurcations in elastic bilayers with modest contrast in modulus. Extreme Mechanics Letters 11:30-36

39. Zhao R, Diab M, Kim KS (2016) The primary bilayer ruga-phase diagram ii: Irreversibility in ruga evolution. Journal of Applied Mechanics 83:
40. Tallinen T, Biggins JS (2015) Mechanics of invagination and folding: Hybridized instabilities when one soft tissue grows on another. Physical Review E 92:022720
41. Diab M, Zhang T, Zhao R, Gao H, Kim K-S (2013) Ruga mechanics of creasing: From instantaneous to setback creases. Proceedings of the Royal Society A: Mathematical, Physical and Engineering Sciences 469:20120753
42. Brau F, Damman P, Diamant H, Witten TA (2013) Wrinkle to fold transition: Influence of the substrate response. Soft Matter 9:8177-8186
43. Bayley FA, Liao JL, Stavrinou PN, Chiche A, Cabral JT (2014) Wavefront kinetics of plasma oxidation of polydimethylsiloxane: Limits for sub-μm wrinkling. Soft Matter 10:1155-1166
44. Cai S, Breid D, Crosby AJ, Suo Z, Hutchinson JW (2011) Periodic patterns and energy states of buckled films on compliant substrates. Journal of the Mechanics and Physics of Solids 59:1094-1114
45. Hutchinson JW (2013) The role of nonlinear substrate elasticity in the wrinkling of thin films. Philos Trans A Math Phys Eng Sci 371:20120422
46. Zang J, Zhao X, Cao Y, Hutchinson JW (2012) Localized ridge wrinkling of stiff films on compliant substrates. Journal of the Mechanics and Physics of Solids 60:1265-1279
47. Cao Y, Hutchinson JW (2011) From wrinkles to creases in elastomers: The instability and imperfection-sensitivity of wrinkling. Proceedings of the Royal Society A: Mathematical, Physical and Engineering Sciences 468:94-115
48. Bowden NH, Wilhelm T. S., Paul KE, Whitesides GM (1999) The controlled formation of ordered, sinusoidal structures by plasma oxidation of an elastomeric polymer. APPLIED PHYSICS LETTERS 75:2557-2559
49. Wang Q, Zhao X (2015) A three-dimensional phase diagram of growth-induced surface instabilities. Sci Rep 5:8887
50. Wang Q, Zhao X (2013) Creasing-wrinkling transition in elastomer films under electric fields. Physical Review E 88:042403
51. Zhao R, Zhao X (2017) Multimodal surface instabilities in curved film–substrate structures. Journal of Applied Mechanics 84:
52. Zhang Z, Liu M, Ibrahim MM, Wu H, Wu Y, Li Y, Mersal GAM, El Azab IH, El-Bahy SM, Huang M, Jiang Y, Liang G, Xie P, Liu C (2022) Flexible polystyrene/graphene composites with epsilon-near-zero properties. Advanced Composites and Hybrid Materials 5:1054-1066
53. Xie P, Shi Z, Feng M, Sun K, Liu Y, Yan K, Liu C, Moussa TAA, Huang M, Meng S, Liang G, Hou H, Fan R, Guo Z (2022) Recent advances in radio-frequency negative dielectric metamaterials by designing heterogeneous composites. Advanced Composites and Hybrid Materials 5:679-695
54. Liu M, Wu H, Wu Y, Xie P, Pashameah RA, Abo-Dief HM, El-Bahy SM, Wei Y, Li G, Li W, Liang G, Liu C, Sun K, Fan R (2022) The weakly negative permittivity with low-frequency-dispersion behavior in percolative carbon nanotubes/epoxy nanocomposites at radio-frequency range. Advanced Composites and Hybrid Materials 5:2021-2030
55. Xie P, Liu Y, Feng M, Niu M, Liu C, Wu N, Sui K, Patil RR, Pan D, Guo Z, Fan R (2021) Hierarchically porous co/c nanocomposites for ultralight high-performance microwave absorption. Advanced Composites and Hybrid Materials 4:173-185
56. Lei J, Fan J, Yu C, Zhang L, Jiang S, Tu B, Zhao D (2004) Immobilization of enzymes in mesoporous materials: Controlling the entrance to nanospace. Microporous and Mesoporous Materials 73:121-128
57. Zhang Y, Wang L, Zhao L, Wang K, Zheng Y, Yuan Z, Wang D, Fu X, Shen G, Han W (2021) Flexible self-powered integrated sensing system with 3d periodic ordered black phosphorus@mxene thin-films. Adv Mater 33:e2007890

58. Wang D, Cheewaruangroj N, Li Y, McHale G, Jiang Y, Wood D, Biggins JS, Xu BB (2018) Spatially configuring wrinkle pattern and multiscale surface evolution with structural confinement. Advanced Functional Materials 28:1704228
59. Lawton RA, Price CR, Runge AF, Doherty WJ, Saavedra SS (2005) Air plasma treatment of submicron thick pdms polymer films: Effect of oxidation time and storage conditions. Colloids and Surfaces A: Physicochemical and Engineering Aspects 253:213-215
60. Nania M, Foglia F, Matar OK, Cabral JT (2017) Sub-100 nm wrinkling of polydimethylsiloxane by double frontal oxidation. Nanoscale 9:2030-2037
61. Nania M, Matar OK, Cabral JT (2015) Frontal vitrification of pdms using air plasma and consequences for surface wrinkling. Soft Matter 11:3067-3075
62. Allen HG. *Analysis and design of structural sandwich panels*. (Pergamon Press; 1969), pp.
63. Genzer J, Groenewold J (2006) Soft matter with hard skin: From skin wrinkles to templating and material characterization. Soft Matter 2:310-323
64. Huang ZY, Hong W, Suo Z (2005) Nonlinear analyses of wrinkles in a film bonded to a compliant substrate. Journal of the Mechanics and Physics of Solids 53:2101-2118
65. Biot MA. *Mechanics of incremental deformations*. (John Wiley & Sons, Inc.; New York, 1965), pp.
66. Koiter WT. A transiation of the stability of elastic equilibrium. (1945)
67. Zhao R, Zhang T, Diab M, Gao H, Kim KS (2015) The primary bilayer ruga-phase diagram i: Localizations in ruga evolution. Extreme Mechanics Letters 4:76-82
68. Bruzewicz DA, Reches M, Whitesides GM (2008) Low-cost printing of poly(dimethylsiloxane) barriers to define microchannels in paper. Analytical Chemistry 80:3387-3392